Contents lists available at ScienceDirect

International Journal of Naval Architecture and Ocean Engineering
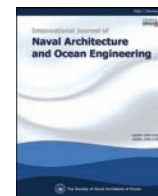
Design, test and numerical simulation of a low-speed horizontal axis hydrokinetic turbine

Wenlong Tian [a, b, *], Zhaoyong Mao [a, b], Hao Ding [c]

[a] School of Marine Science and Technology, Northwestern Polytechnical University, Xi'an, 710072, China
[b] Key Laboratory for Unmanned Underwater Vehicle, Northwestern Polytechnical University, Xi'an, 710072, China
[c] School of Mechanic and Electronic Engineering, Henan University of Technology, Zhengzhou, 450001, China

ARTICLE INFO

ABSTRACT

A small-scale horizontal axis hydrokinetic turbine is designed, manufactured and studied both experimentally and numerically in this study. The turbine is expected to work in most of China's sea areas where the ocean current velocity is low and to supply electricity for remote islands. To improve the efficiency of the turbine at low flow velocities, a magnetic coupling is used for the non-contacting transmission of the rotor torque. A prototype is manufactured and tested in a towing tank. The experimental results show that the turbine is characterized by a cut-in velocity of 0.25 m/s and a maximum power coefficient of 0.33, proving the feasibility of using magnetic couplings to reduce the resistive torque in the transmission parts. Three dimensional Computational Fluid Dynamics (CFD) simulations, which are based on the Reynolds Averaged Navier—Stokes (RANS) equations, are then performed to evaluate the performance of the rotor both at transient and steady state.

1. Introduction

In recent years, the exploitation of renewable energy is getting more and more popular with the rapid development of industrial economy and the growing consumption of fossil fuels. Among the various kinds of renewable energies, hydrokinetic energy has the advantages of high energy density, large reserves and ease of developing and attracts growing interests. Hydrokinetic energy is the kinetic energy in moving water such as the river, tide and ocean current. Hydrokinetic turbines are the devices for converting the hydrokinetic energy into electricity. According to the relative direction between the turbine rotation axis and the flow, hydrokinetic turbines can be classified into two main categories, Horizontal Axis Hydrokinetic Turbines (HAHTs) and Vertical Axis Hydrokinetic Turbines (VAHTs). The HAHTs are more favored due to their high power efficiency.

Several HAHTs have been successfully developed for commercial applications, such as the SeaGen (MCT, 2017), Alstom (2013) and HS1000 (Tethys, 2011). These commercial devices are usually large in size and power, with blade length near 10 m and rated power on the order of megawatt, and are often planted in mid-to-large scale arrays for large-scale power output. However, the development of small-scale HAHTs is not so successful mainly because of the small economic market. But small-scale HAHTs are well suited for usmall-scale power generation situations, such as lighthouses and remote islands where electricity cables can not reach. Therefore it is meaningful to develop a small-scale HAHT for these places.

The most important factor limiting the development of small-scale HAHTs is the ocean current velocity. Conventional commercial HAHTs are often installed in carefully selected straits where the ocean current velocity is high. But the area of the high-speed straits is small compared to the whole sea area. Take for example the distribution of ocean current energy resources in China. The ocean current velocity in the east entrance of the Qiongzhou Strait is in the range of 2.0—2.5 m/s, but the currents velocity is less than 0.77 m/s in most areas of Bohai Sea and is in the range of 0.5—1.0 m/s in most areas of the Yellow Sea (Wang et al., 2011). Small-scale HATTs are more likely to be planted where sustained power is needed, like the lighthouses, rather than places where ocean current velocities are high. Therefore, the low-speed velocity precondition must be considered in the design of small-scale HATTs.

In conventional HATTs, mechanical seals are commonly applied on the generator shafts to avoid the seepage and corrosion of the seawater. However, the mechanical seal increases the friction torque. Since the torque of the turbine rotor is proportional to the square of the flow velocity, the rotor torque gets smaller and the proportion of the friction increases at lower flow velocities, resulting in the decrease of the efficiency of the system. Therefore, to improve the efficiency of low-speed HAHTs, work should be done on increasing the rotor torque and reducing the resistive torque.

In the aspect of increasing the rotor torque, the duct augmented designs have attracted research interest for many years. The duct, or diffuser, works to increase the mass flux through the rotor and enhance the performance of turbines. The ducts can be classified into two categories based on the shape, the uni-directional type (Cresswell et al., 2015) and the bi-directional type (Fleming and Willden, 2016). The optimization of the duct shape to maximize the power of the turbine has always been a research hotspot in the previous studies (Fleming et al., 2011; Gaden and Bibeau, 2010; Luquet et al., 2013; Shives and Crawford, 2010). Comprehensive reviews of research on the ducted turbines are presented in (Belloni and Clarissa, 2013; Fleming and Willden, 2016).

While in the aspect of reducing resistive torque, especially the torque brought by the mechanical seal, some researchers tried to reduce the seal drag by changing the surface of the seal ring. Xu et al. compared the drag of a bionic non-smooth seal ring and that of a common smooth one (Xu et al., 2015), they found that the non-smooth surface resulted in a maximum drag reduction of 15%. Similar studies can also be found in these references (Gu et al., 2013; Liu and Wang, 2014). It should be noted that although the drag can be reduced, the drag-reduction ratio is relatively small. To completely eliminate the drag or torque brought by seal, in this study, a magnetic coupling is used for the non-contacting transmission of the rotor torque and the resistive torque of the mechanical seal is avoided.

A number of researchers developed and experimentally tested HAHTs and most of these experimental studies focused on the performance of the rotor alone, which was driven by a motor and rotated at constant rotational speed (Bahaj et al., 2007; Doman et al., 2015; Galloway et al., 2011; Morandi et al., 2016; Mycek et al., 2014a, b; Seo et al., 2016). Morandi et al. tested a 1/25 scale turbine in a circulating water channel and compared the power coefficient of the turbine at different flow velocities (Morandi et al., 2016). Bahaj et al. carried out a power and thrust coefficient study on a 0.8 m-diameter turbine in a towing tank and in a cavitation tunnel, providing comprehensive high-quality data for the validation of numerical computations (Bahaj et al., 2007). Galloway et al. studied the power and thrust performance of a 1/20th scale turbine operating at yaw and in wave by performing towing tank experiments (Galloway et al., 2011). Mycek et al. studied the upstream turbulence intensity effect and the interaction between two turbines, with emphasis paid on the wake of the turbine (Mycek et al., 2014a, b).

A few researchers performed field tests of HAHT prototypes which contain the rotor, gears and the generator. Jeffcoate et al. conducted experiments to study the interactions between two 1.5 m diameter turbines and the performance of the turbines were evaluated at different relative locations (Jeffcoate et al., 2016). Atcheson et al. presented experiments measuring the performance and wake characteristics of a 1/10th turbine in a towing tank and a maximum power coefficient of 0.35 was obtained at a towing speed of 1.2 m/s (Atcheson et al., 2015).

Except for experimental tests, the Computational Fluid Dynamics (CFD) method is commonly used in the prediction of the hydrodynamic performance and wake characteristics of HATTs due to its high accuracy and low cost. Comprehensive CFD simulations of HATT have been created. Tian et al. provided detailed information on the modeling of a 1/20th scale HATT and numerically studied the influences of upstream turbulence intensity and yaw angle on the turbine performance (Tian et al., 2016). Lawson et al. modeled numerically a 20 m-tidal turbine at different flow velocities using the commercial CFD code STAR CCM+, including an analysis of the effect of grid density and time step on the calculated torque (Lawson et al., 2011). Schleicher et al. designed a novel portable micro-hydrokinetic turbine and characterized the performance of the turbine with a RANS method (Schleicher et al., 2014). Lee et al. studied the effect of the distance between dual rotors on the performance and efficiency of a counter-rotating tidal turbine using both CFD and experimental methods (Lee et al., 2016). Liu et al. studied the wakes of a horizontal axis ocean current turbine with three different RANS methods, the results show that the Sliding Mesh Method is more accurate than the Moving Reference Frame and the Actuator Disk Model (Liu et al., 2016). Tatum et al. studied the performance of a HATT subjected to profiled flow and the surface gravity waves (Tatum et al., 2016). Wang et al. analyzed the hydrodynamic performance of a turbine with multi-degree of freedom (rotation, rolling, surging) coupled motions (Wang et al., 2016).

The aim of this study is to design and test of a low-speed HAHT which is expected to work in most of China's sea areas and supply electricity for lighthouses and residents on remote islands. The low flow speed considered here is 0.5 m/s according to the distribution of ocean current energy resources in China (Wang et al., 2011). The structure design, experimental test and numerical simulations of the turbine are described in detail in the following content. The performances of the turbine at both transient and steady state are evaluated.

2. Design of the turbine

2.1. Overview

The low-speed HAHT designed in this study is a three-bladed, 1.2 m diameter turbine (Fig. 1) with a rated power of 30 W at a rotor speed of 40 rpm and an upstream velocity of $V = 0.5$ m/s. The HAHT is mainly composed of a three-bladed rotor, a hub, a Magnetic Coupling (MC) and a generator. The blades are mounted on the hub and the torque of the rotor is transmitted to the generator via the MC, which is composed of an external rotor, an isolation hood and an internal rotor. The external rotor is connected with the power shaft and the internal rotor is connected with the gearbox. The isolation hood separates the rear parts from the seawater, forming a sealed chamber in which the gearbox and the generator is mounted. Because the shaft of the generator is isolated from the seawater, the mechanical seal and the brought seal friction are avoided.

2.2. Rotor design

The rotor is the first-stage energy conversion unit of the hydrokinetic turbine and its efficiency directly determines the overall efficiency of the turbine. In this study, the HarpOpt rotor design code is used for the optimal design of the rotor. HarpOpt is one of the most successful rotor design code based on the Blade Element Momentum (BEM) method and has been widely used in the design of wind/water rotors (Sale, 2014). The rotor designed in this study is fixed-pitched, three-bladed, with a diameter of $D = 1.2$ m and a hub diameter of 0.12 m. The airfoil shapes used by this rotor were created from the FF-77-W airfoil type (Althaus, 1996); more specifically they were interpolated from the fx77w121, fx77w153, and
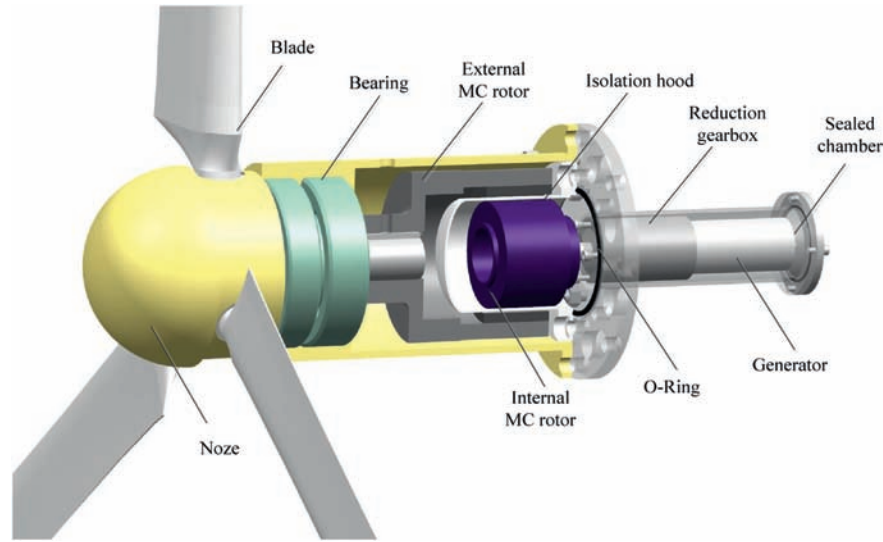
Fig. 1. Solid view of the HAHT.

fx77w258 airfoil geometries provided available at (UIUC, 2011). The Prandtl model is used to correct the effects of the tip loss and the hub loss. The rotational wake effect is also considered in the optimization. As for the stall delay models, the lift and the drag coefficients are corrected via the Selig/Du method. The rotor is optimized for the maximum efficiency at a constant RPM of 40, corresponding to a tip speed ratio of 5 at an inflow velocity of 0.5 m/s. The details of the utilized blade geometry are summarized in Table 1, where r is the spanwise location, φ is the blade twists angle, c is the chord length, t is the thickness of the blade. The airfoil starts from a spanwise location of $r/R = 0.108$ and in the region of $0.1 < r/R < 0.108$, the blade section transfers from a circle to an airfoil.

2.3. MC design

The MC allows torque transfer between the magnetic rotors without mechanical contacting. A concentric MC is designed in this study. 8 neodymium-iron-boron magnetic poles are arranged concentrically on the external and the internal magnetic rotors (Fig. 2). Fig. 2(a) shows the positions of the poles at the no-load state, where the north and the south poles on the magnetic rotors are aligned and attracted to each other, resulting with zero torque. While at the on-load condition shown in Fig. 2(b), a deflection angle exists between the two rotors and the circumferential components of the attractive and the repulsive forces between the magnetic poles drives the rotation of the internal rotor.

Table 1
Detailed blade description.

r/R	φ (deg)	c/R	t/c (%)
0.108	14.61	0.096	25.6
0.138	14.57	0.093	24.9
0.196	14.47	0.091	23.5
0.278	14.27	0.088	21.6
0.379	13.81	0.087	19.3
0.492	12.93	0.085	16.6
0.608	11.58	0.084	14.8
0.721	9.75	0.083	13.8
0.822	7.61	0.082	12.9
0.904	5.52	0.081	12.2
0.962	3.79	0.081	12.1
1.000	2.90	0.081	12.1

The designed MC has a diameter of 0.112 m and a length of 0.120 m, and is capable of transmitting a maximum torque 24Nm, which is two times of the rotor torque predicted by the HarpOpt and can ensure the safety of torque transmission.

2.4. Generator and gearbox

The permanent magnet generators have the advantages of simpler structure, smaller volume and mass over the electrically excited generators. In this design, a permanent magnet DC generator, the 24 V Maxon 35 L, is used. The rated power and speed of the generator are 80 W and 7160 rpm, respectively. In order to match the speeds of the rotor and the generator, a 3-stage planetary reduction gearbox, GPX 42, which has a reduction ratio of 1/156, is selected. The main parameters of the Maxon 35 L generator and the GPX 42 gear box can be found on the website (Maxon, 2017).

3. Experiment setup

3.1. The prototype and the test tank

A prototype of the HAHT is manufactured for the experimental test, as shown in Fig. 3. The nose and the blades are machined from T7075 aluminum alloy on a computer numerical control machine to an order of accuracy of ±0.05 mm. The other parts of the turbine is made of T304 stainless steel. The test tank is a towing tank at Wuhan University of Technology, with a length of 132 m and a width of 10.8 m. The depth of the towing tank is 2.0 m and the turbine is placed in the middle of the tank with a distance of 0.4 m to the surface of the water, resulting with a blockage ratio of 5%. It should be noted that the blockage ratio of the CFD domain in Section 4 is 3%. The blockage ratios of the towing tank and the CFD domain are rather small so that the boundary effect is insignificant. Fig. 3 shows the turbine installed on the carriage.

3.2. Post processing

Tip speed ratio represents the ratio of the blade tip speed to the upstream flow speed, and has the following expression,
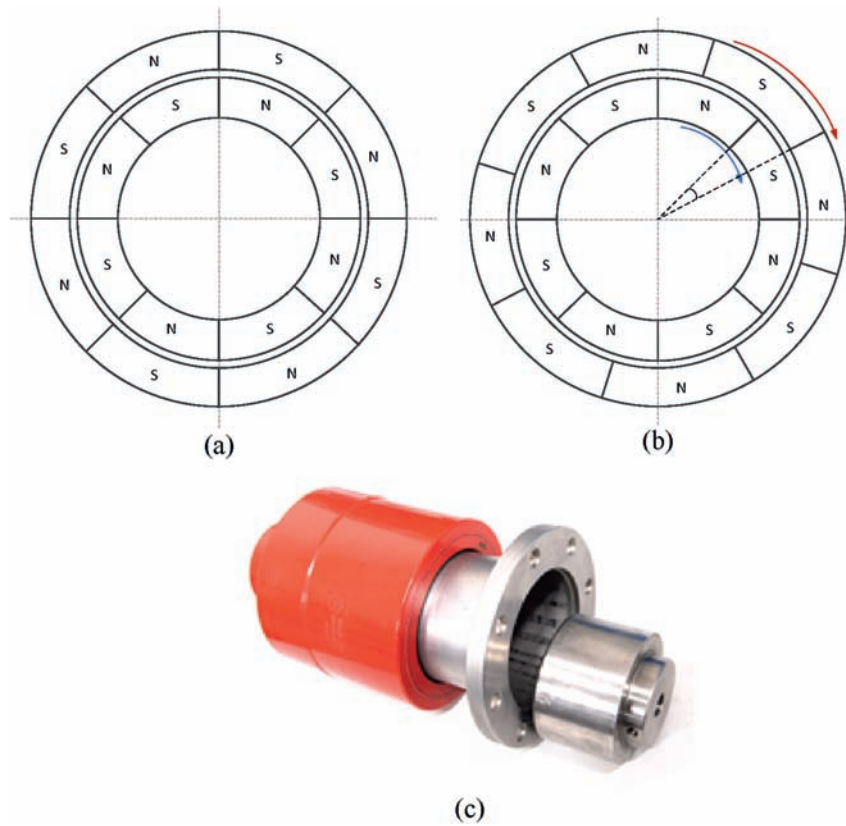
$$TSR = \frac{\omega R}{V}. \tag{1}$$

Fig. 2. Magnetic poles distribution for (a) the no-load and (b) the on-load conditions and (c) photograph of the magnetic coupling.
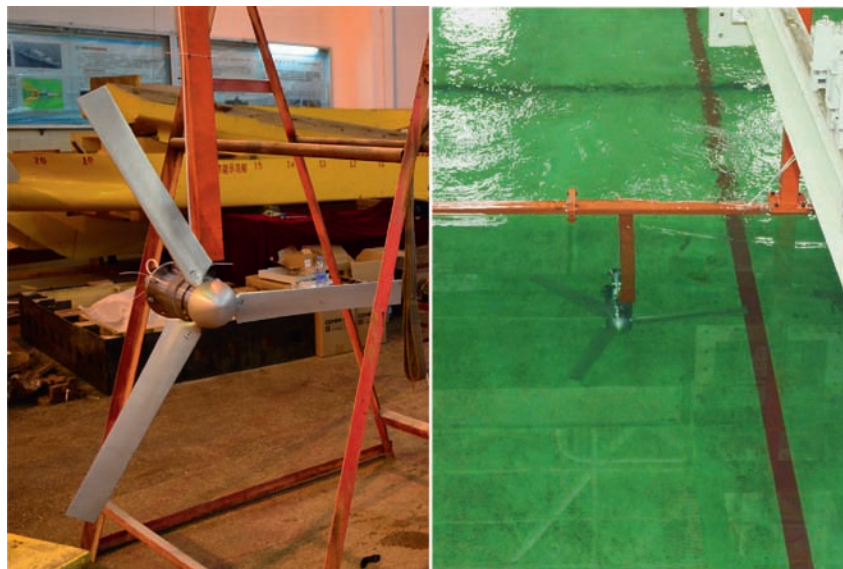

Fig. 3. Photograph of the HAHT prototype.

The torque, thrust and power of the rotor are normalized in the following way:

$$C_t = \frac{T}{0.5\rho\pi R^2 V^2},\qquad(3)$$

$$C_m = \frac{M}{0.5\rho\pi R^3 V^2},\qquad(2)$$

$$C_P = \frac{P}{0.5\rho\pi R^2 V^3},\qquad(4)$$

where M, T and P are the torque, thrust and power of the rotor, respectively.

In the towing tank tests, the velocity of the carriage was stabilized at 0.5 m/s. A load resistor was added on the generator and the rotor speed was controlled by changing the value of the resistor. The voltage across the resistor was measured and recorded by a Tektronix DPO4104B oscilloscope with a sampling rate of 500 Hz.

The rotor speed is estimated using the following equation:

$$\omega = \frac{K_v(U + R_0 U/R)}{k}, \tag{5}$$

where K_v is the motor velocity constant and is 326 rpm/V for the Maxon 35 L generator, R_0 is the terminal resistance of the generator and is equal to 0.346Ω, R is the load resistor, U is the voltage across the resistor, k is the reduction ratio of the gearbox.

The power of the HAHT is calculated by

$$P = \frac{U^2}{R}. \tag{6}$$

4. Numerical model

The CFD model is built in the ANSYS v15.0 environment (ANSYS, 2011). The grids are generated using the ICEM utility and the transient simulations are performed using the FLUENT code. The incompressible RANS equations are solved with a second-order-accurate finite-volume discretization scheme. The shear stress transport (SST) $k - \omega$ turbulence model is selected to model the turbulence terms of the RANS equations.

4.1. Computing domain and grids

The computation domain is a cylinder with a diameter of 6D and a length of 12D. The rotor is placed in the centerline of the cylinder and at a distance of 4D from the left boundary, as shown in Fig. 4. The hub of the turbine, which has little effect on the torque, is ignored in the numerical model considering the complexity of structure and economy of computation time. The overall domain is split into two subdomains, including a rotor domain containing the cells surrounding the rotor and a outer domain containing the elements in the outer region.

The boundary conditions are also shown in Fig. 4. A uniform velocity inlet boundary is applied at the left surface of the domain. A pressure outlet boundary is applied at the right surface of the domain. To improve the stability of the numerical simulations, symmetry boundary conditions are applied at the side wall of the cylinder. No-slip boundary conditions are imposed at the surface of the blades. The overlapped faces between the two subdomains are set as interfaces.

Structured grids are generated using the ICEM grid generation utility. The grids of the two subdomains are generated separately and then merged together. As can be seen in Fig. 4, the grids near
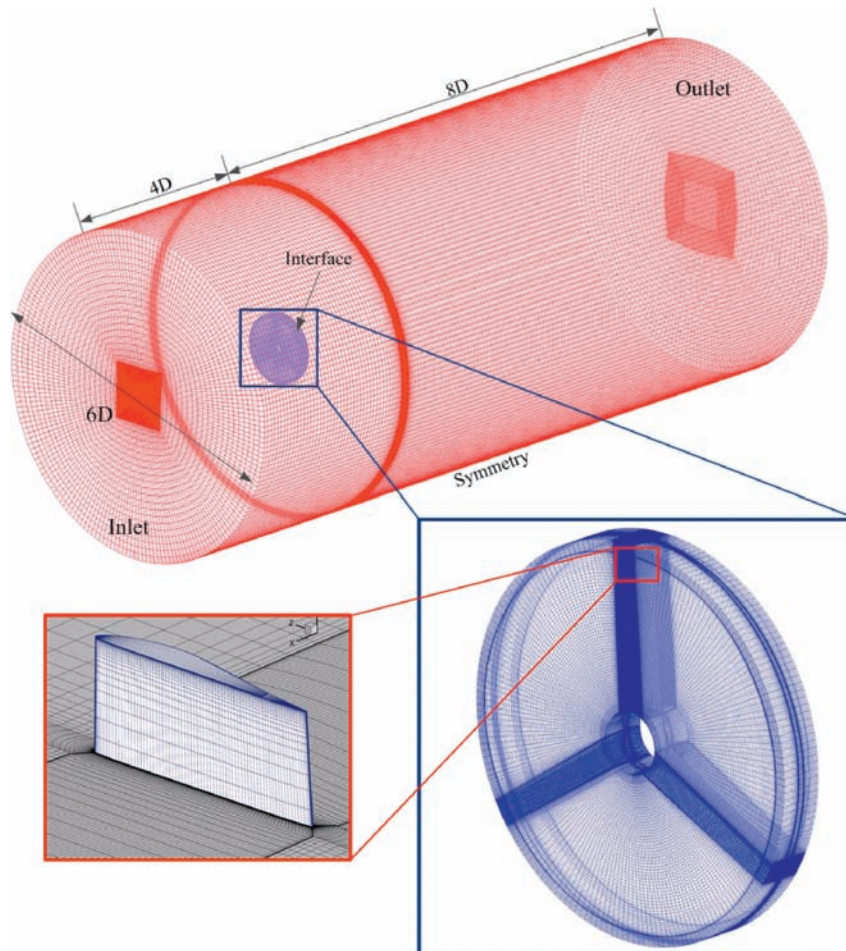

Fig. 4. Domain, boundary conditions and the mesh.

the rotor, where high velocity gradients are expected, have a higher grid node density. Prism layer grid elements are applied on the blade surfaces to provide sufficient precision to describe the boundary layer flow. The Reynolds number is approximately 0.6×10^6 considering the rotor diameter and the inflow velocity. The height of the first prism layer above the surfaces of the blades is set as 0.02 mm so that the y^+ value for the first layer of elements from the wall is around 1, which is suitable for the SST $k - \omega$ turbulence model. A global growth rate of 1.2 is chosen for all the grids.

4.2. Solution setup

Simulations are carried out for *TSR*s varying from 2 to 8. A sliding mesh model is used to simulate the rotation of the rotor. The torque and thrust of the rotor is monitored during the simulation. It is observed that the forces of the rotor maintain stable after three to four revolutions, therefore, each of the simulations in this study lasts for six revolutions to allow the convergence of the forces on the rotor. The mean performances of the rotor, including thrust and power, are averaged using the data in the last revolution. The time step for each simulation is set so that $1°$ of rotor rotation is achieved each time step. The drop of all scaled residuals below 1e-4 is utilized as the convergence criterion. In order to obtain a fast convergence, the pressure–velocity coupling method is used in all simulations. A Second Order Upwind spatial discretization algorithm is used for all the equations to produce more accurate results.

4.3. Verification and validation

A grid resolution study is performed to evaluate the influence of grid resolution on the power and thrust of the rotor. The simulations are conducted at *TSR* = 5. Table 2 summarizes the results with different grid resolutions. It can be seen that grids with approximately 7.8 million and 10.3 million elements give approximately the same results. This indicates that further increasing the grid resolution would not significantly affect the CFD results. Considering the economy of time in the simulation, the grid with 7.8 million elements is chosen for the following simulations.

In this study, the experiments are carried out with the whole HAHT including the transmission parts and the generator, but the CFD simulations are performed with the rotor. In order to validate the numerical method, a validation study is performed on an existing tidal rotor tested in a cavitation tunnel, as listed in Table 3 (Bahaj et al., 2007). Fig. 5 shows a comparison of the coefficients of power using this CFD approach and the experimental results over a range of tip speed ratio. It can be seen that the coefficients of power are in very good agreement with the experimental results, except
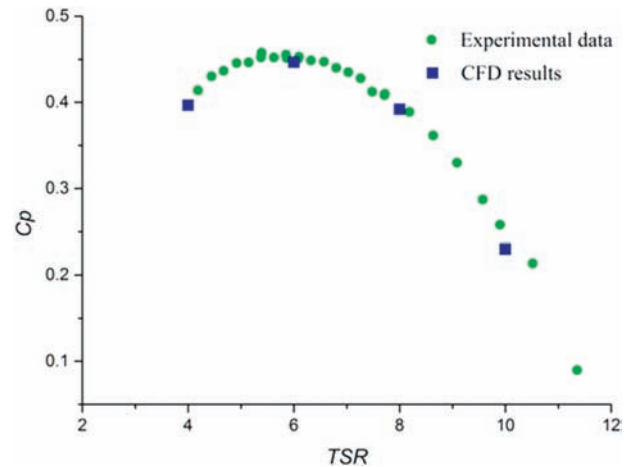
Table 2
Results of torque and thrust for mesh verification.

Approx. number of grid elements (million)	C_p	C_t
5.6	0.405	0.723
7.8	0.410	0.729
10.3	0.411	0.731

Table 3
Settings for the numerical method validation.

Parameters	Value
Number of blades	3
Blade section	NACA63-8XX
Diameter	0.8 m
Inflow velocity	1.73 m/s
TSR	5–10

Fig. 5. Results of the numerical method validation.

that for *TSR* = 10 the C_p coefficient is underestimated with a relative error of 8%. Overall, the numerical method in the present study has predicted results with acceptable accuracy.

5. Results and discussion

5.1. Rotating performance of the turbine

In the experiments, the rotation velocity of the rotor is controlled by adjusting the value of the load resistance and the voltage on the resistance is recorded. The measured voltage of a 10Ω load resistance is taken as an example, as shown in Fig. 6. It can be seen from the Fig. that the voltage converges with fluctuation and maintains nearly stable after 100s. Each test lasts for 140s and the data in the last 10s is averaged to calculate the final load voltage.

To measure the performance of the turbine at different rotation velocities, tests are carried out for load resistances ranging from 6Ω to 25Ω. The rotation velocity of the turbine changes with the load resistance and is then estimated by Eq. (5). The voltage and the calculated rotation velocity are plotted against the load resistance, as shown in Fig. 7. The voltage increases nonlinearly with the resistance, and the growth rate decreases gradually. The increase in load resistance reduces the output current and the resistive torque, therefore the rotor of the generator rotates faster. The data presented in Fig. 7 may help validating the future numerical model of a whole turbine system including the rotor, transmission parts and the generator.

To investigate the relationship between the performance of the turbine and the *TSR*, CFD simulations at *TSR*s ranging from 2 to 8 are evaluated. While for the experimental test, the *TSR* varies from 3.56 to 6.65 as the load of the generator changes. Fig. 8 presents the comparison of the rotor power coefficients obtained from the experiments, CFD simulations and the BEM method (HarpOpt). Among the three methods, the BEM predicts the highest C_p curve. The C_p predicted by BEM increases with *TSR* up to *TSR* = 4.65 and then decreases, with a peak C_p value of 0.45. The C_p curve obtained by CFD shows nearly the same shape with the BEM, but is lower and has a smaller peak C_p (0.41, obtained at *TSR* = 5). The main reason for the differences in the results of the BEM and the CFD method is that the BEM method fails to consider the viscous and dissipative effects which are important at low velocities. Due to these effects, the performances of hydrokinetic turbines are degraded at low velocities. A previous experimental study showed that the
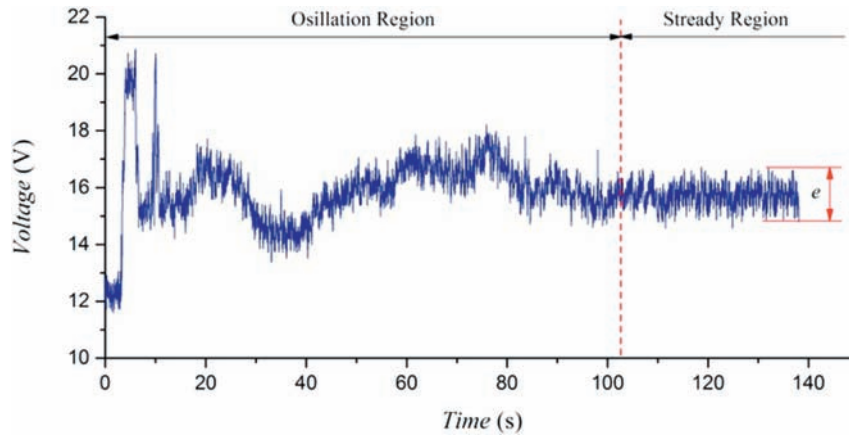
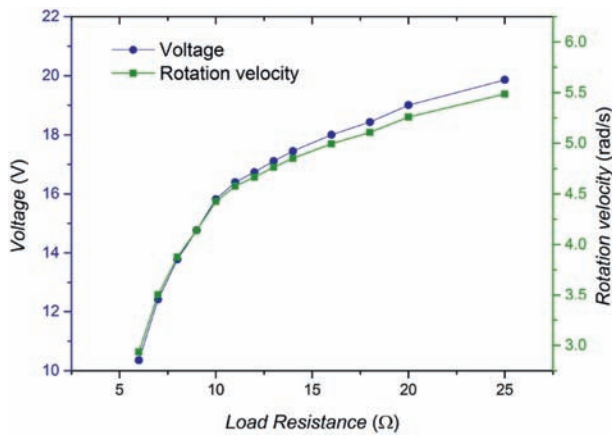**Fig. 6.** Time history of the load voltage.

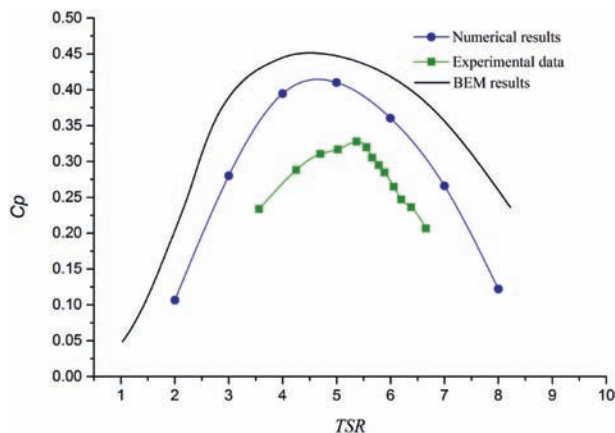**Fig. 7.** Variation of voltage and rotor speed with the load resistance.

Fig. 8. Coefficient of power of the HAHT obtained by BEM, CFD and experimental method.

efficiency of a HAHT reduced by approximately 15% when the flow velocity decreases from 1.52 m/s to 0.78 m/s (Morandi et al., 2016), similar comparisons can also be find in (Doman et al., 2015; Mycek et al., 2014a). The C_p curve of the experimental tests is the lowest among the three, with a peak value of 0.33. Another difference is that the TSR corresponding to the peak C_p for the tests is slightly larger than that of the CFD, with a value of 5.37. The main reason for

the differences in the peak C_p of the CFD and the experimental method is that the CFD simulations only consider the efficiency of the rotor alone, and the efficiency of the generator and the energy loss caused by bearings and gears are neglected.

It should be added that the chance of cavitation is higher at TSR greater than 5. The optimal TSR of the present rotor is relatively higher mainly because of the consideration that the rotor could match better with the rated speed of the generator. The Maxon 35 L generator has a rated speed of 7160 rpm. After the reduction of the GPX 42 gear box that has a reduction ratio of 1/156, the rated speed is reduced to approximately 46 rpm, which is close to the optimal RPM of the rotor design (40 rpm).

Because the experiments only measure the power of the tidal rotor, the results for the thrust are obtained using the CFD and BEM approach. Fig. 9 shows the variation of the C_t with the TSR. The predicted C_t increases with TSR and then decreases with increasing TSR. The BEM method calculates a higher C_t than CFD when $TSR \leq 6$. The peak C_t for the BEM and the CFD are 0.79 and 0.73, respectively. The TSR for the peak C_t is also where the turbine generates the peak power. There are two main reasons for the inconsistency between the CFD and the BEM results. Firstly, the nacelle and the hub of the turbine is not modeled in the CFD method (as mentioned in Section 4.1), therefore the thrust on the nacelle and the hub is ignored and the thrust predicted by CFD is smaller than that by the BEM method when $TSR \leq 6$. Secondly, the BEM method lacks the ability to accurately model swirling flows at higher $TSRs$, so it predicts a smaller
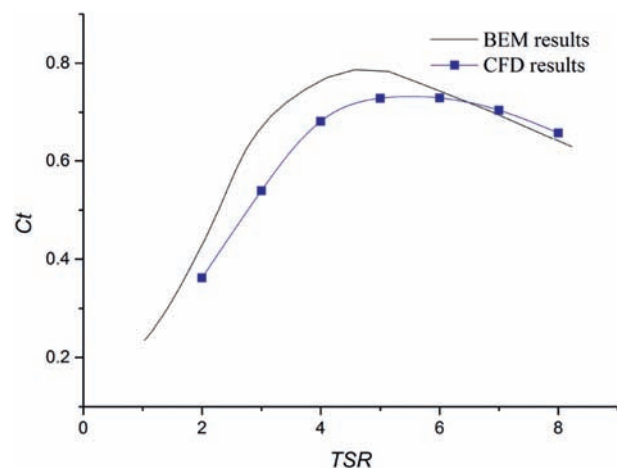

Fig. 9. Coefficient of torque of the HAHT obtained by BEM and CFD method.
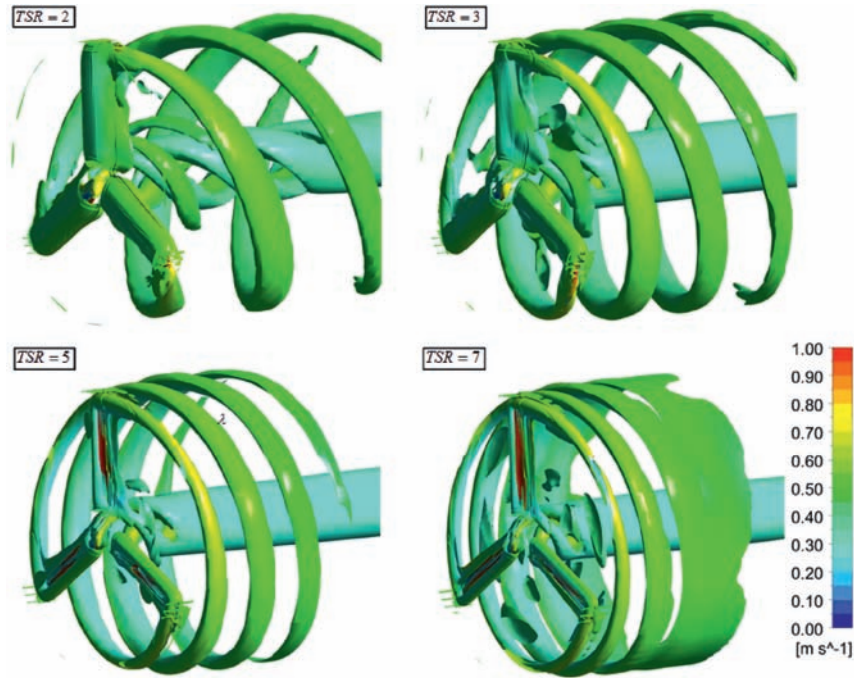
Fig. 10. Vortical structures using iso-surfaces of Q = 0.1 and colored with magnitude of velocities for different *TSR*s.

thrust where the rotor rotates at a faster speed.

For better understanding the flow characteristics at different *TSR*s, the vortical structures are shown in Fig. 10. The vortical structures are plotted using iso-surfaces of the second invariant of the rate of strain tensor at Q = 0.1 and colored with the magnitude of velocity. Flow separations are observed at the tips of the blades, where strong vortices are shed from the blade tips like spiral lines with a diameter slightly larger than that of the rotor. With the increase of the *TSR*, the pitch of the spiral vortices decreases and at *TSR* = 7, the tip vortices merge into a cylindrical surface which dissipates quickly downstream of the rotor. Vortices also detach from the roots of the blades and form small spiral vortex lines which are concentric to the tip vortices but have smaller diameters. The root vortices are lower in velocity than the tip vortices but have a larger axial dimension (see Fig. 10).

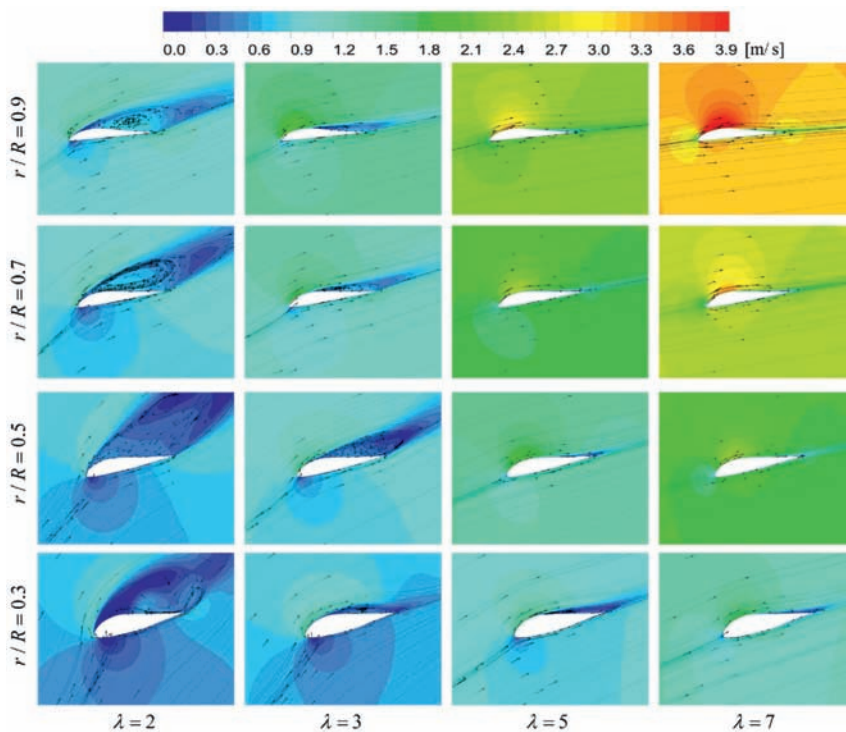To show more clearly the flow around the blade, the velocity

Fig. 11. Velocity contours with streamlines at different *TSR*s and sections of the blade.

contours and streamlines at four blade sections, 30%, 50%, 70% and 90% of the radial distance between the axis of rotation and the blade tips (span), are presented for the four evaluated *TSRs* in Fig. 11. At *TSR* = 2, the blade is in a deep stalled condition along its entire length, suffering from flow separation at the four evaluated blade sections. The structure of the flow separation differs with radial location. At 30% and 50% span, the flow separates from both the leading edge and the trailing edge with two strong contra-rotating vortexes. However, at 70% and 90% span the flow separates from the leading edge and reattaches to the suction side of the blade, forming a large vortex which covers the whole suction surface. At *TSR* = 3, separation flow at the leading edge of the blade is seen along the whole blade, but this separation is weaker than that at *TSR* = 2. At *TSR* = 5, weak separation flow occurs near the trail of the suction surface at 30% span. While at the other three spanwise locations, fully attached flow is seen. At *TSR* = 7, the blade is under fully attached flow conditions at all the sections.

5.2. Starting performance of the turbine

In order to generate maximum power, the turbine should have a good starting performance at low water speeds. The cut-in velocity, which is the water speed whe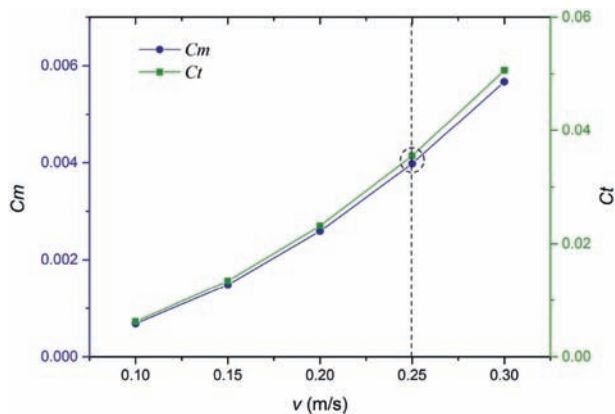re the turbine starts rotating and generating power, is tested experimentally. In the test, the load is removed from the generator and the carriage is accelerated gradually from zero. The velocity is increased with an interval of 0.05 m/s each time if the turbine does not start rotating in 10 s. The final measured cut-in velocity of the designed turbine is 0.25 m/s. This cut-in velocity is considerable lower than common tidal turbines. The low cut-in velocity also proves the feasibility of using magnetic couplings to transmit the torque and reduce friction resistance.

CFD simulations are performed to give a better understanding of the behavior of the turbine at starting. In the simulations, the turbine is fixed and the velocities at the inlet boundary varies from 0.1 m/s to 0.3 m/s. Fig. 12 presents the coefficients of torque and thrust of the turbine at different velocities. The torque and thrust increase approximately quadratically with the flow velocity. At the cut-in speed, the torque coefficient C_m is 0.004, and the corresponding torque is 0.40Nm, which means that the resistance torque caused by the bearings and the gearbox is about 0.40Nm, and that the rotor generates power only when its torque exceeds this value.

For better understanding the flow characteristics near the rotor when starting, the vortical structures for different velocities are shown in Fig. 13. The vortical structures are plotted using iso-surfaces of the second invariant of the rate of strain tensor at Q = 0.1 and colored with the magnitude of velocity. Because the rotor is fixed and the radial velocity is zero (*TSR* = 0), the flow separates directly from both the leading edge and the trailing edge of the blade and forms a wake similar to the Karman vortex street. Moreover, as the inflow velocity increases, the velocity and the influence area of the vortices increase.

Fig. 14 presents the pressure contours at four different blade sections, 30%, 50%, 70% and 90% span, respectively. The pressure is positive on the pressure side of the blade and is negative on the suction side. As the velocity of the incoming flow increases, the pressure increases on the pressure surface but decreases on the suction surface. This is due to the fact that the separation flow on the blades becomes more intense and the vortices have higher velocities as the upstream velocity increases. The increase in the vertical velocities causes a decrease in the local pressure on the suction surface of the blade. As provided in Table 1, the blade is twisted along the spanwise direction. Therefore, the pressure difference on the blade generates a circumferential component which is perpendicular to the flow direction and works as the driven torque to rotate the rotor. With the increase of the flow velocity,
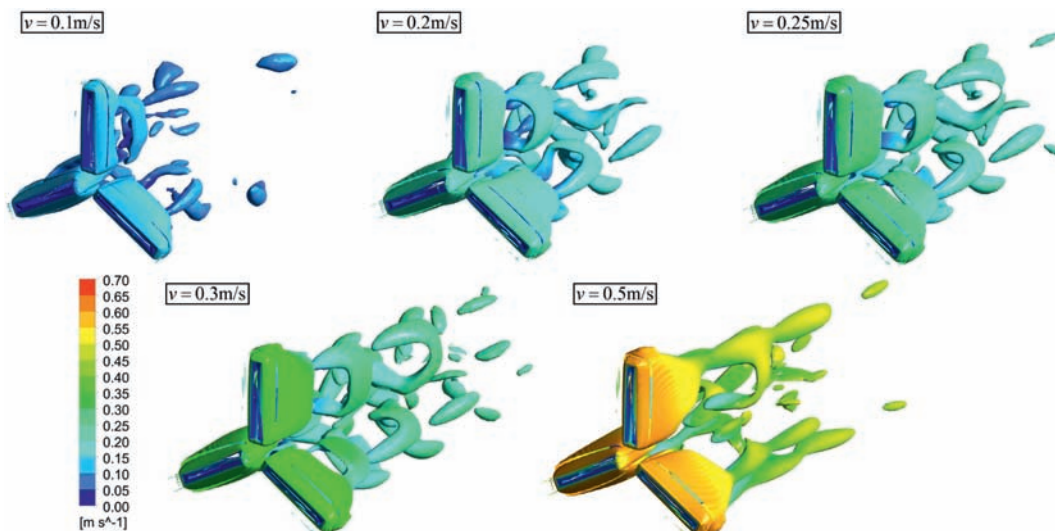

Fig. 12. C_m and C_t of the HAHT at starting.

Fig. 13. Vortical structures around fixed rotors (*TSR* = 0) using iso-surfaces of Q = 0.1 and colored with magnitude of velocities for different flow velocities.
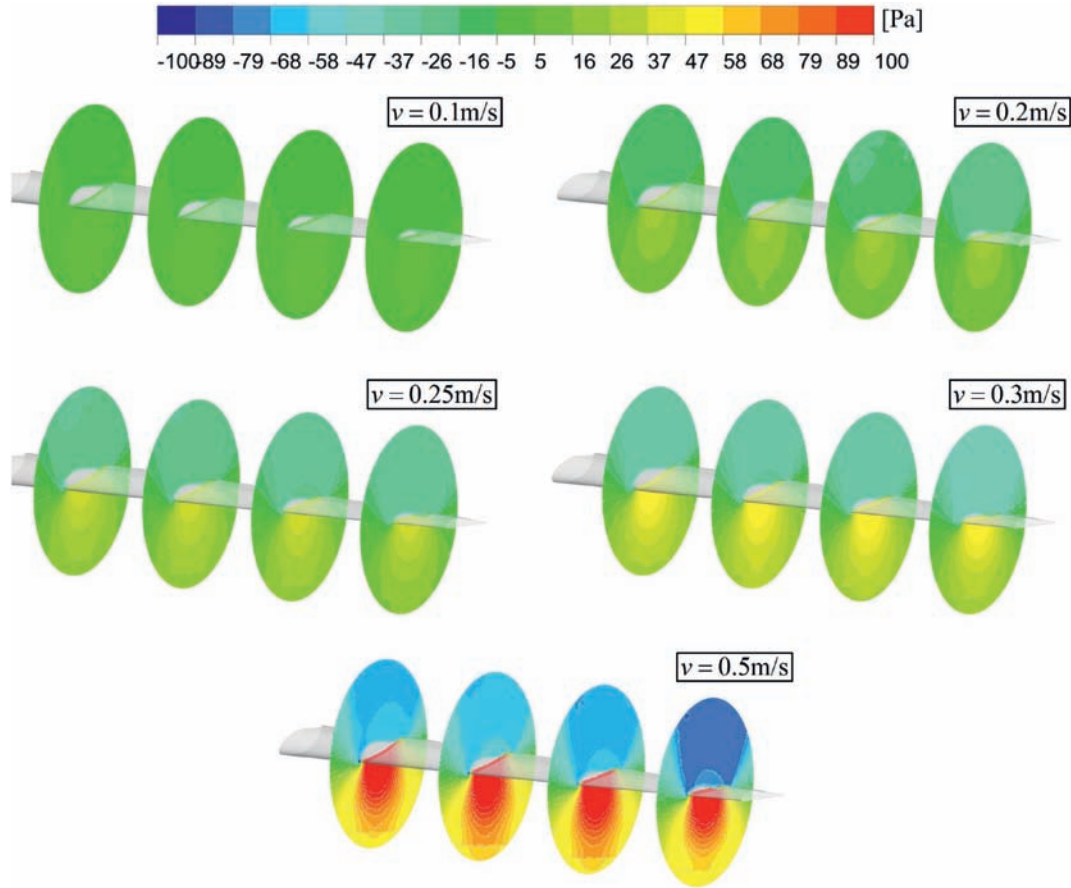
Fig. 14. Pressure contours at different flow velocities and sections of the blade ($TSR = 0$).

this circumferential torque increases, too. This is also the reason for the variation of C_m in Fig. 12.

5.3. Performance comparison with existing HAHTs

In this section, the performance of the present HAHT is quantitatively compared with existing designs. Firstly, the cut-in velocity is compared with that of the SeaGen turbine (see Table 4). The SeaGen turbine at Strangford Lough has a cut-in velocity of 0.8 m/s (Louise et al., 2016) and the cut-in velocity of the present turbine is 0.25 m/s, which is only 31.25% of the SeaGen. Although the SeaGen turbine is much larger in size than the current design, the comparison of the cut-in velocities between these two designs is still reasonable for the following reason. Eq. (2) suggests that the torque is proportional to the product of the cube of rotor radius and the square of the flow velocity,

$$M = C_m 0.5 \rho \pi R^3 V^2 \propto R^3 V^2. \tag{7}$$

To eliminate the dimensional effects, the relative torque can be used to represent the torque per unit length of the rotor on an unit area of the rotor swept area,

Table 4
Comparison of the cut-in velocity.

	SeaGen(Louise et al., 2016)	Present study
Cut-in velocity (m/s)	0.80	0.25

$$M_r = \frac{M}{\pi R^2 R} \propto V^2 \tag{8}$$

Eq. (8) suggests that the relative torque of the turbine is dependent on the square of the flow velocity. Therefore, the cut-in velocity can be considered as a reflection of the relative resistant torque. It is easy to find that the relative resistance torque of the present turbine is only 9.77% of the SeaGen turbine. This means that the resistant torque per unit length and area of the present turbine is 90.33% smaller than that of the SeaGen turbine. This result proves the advantages of using MC to reduce the resistant torque.

The power coefficient of the present HAHT prototype is then compared with the turbine prototypes presented by Jeffcoate et al. (2016). and Atcheson et al. (2015), as listed in Table 5. The C_p of the present turbine is close to the above two prototypes, but it should be noted that our turbine is tested at a flow speed of 0.5 m/s and the previous ones were tested at flow velocities greater than 1 m/s. This result proves the feasibility of using MC to obtain high power performance at low velocities. Table 5 also suggests that the optimal TSR of the present turbine is higher ($TSR = 5.37$) than those provided by Jeffcoate et al. ($TSR = 3$) (Jeffcoate et al., 2016) and Atcheson et al. ($TSR = 3.1$) (Atcheson et al., 2015). The high TSR is chosen for a better match between the rated speed of the generator and the rotor. Although the blades might experience cavitation at higher TSRs due to the increased local velocity, no cavitation was observed in the towing tank test. The reason is that the flow velocity is low (0.5 m/s) and the local velocity of the blade is small even at a high TSR.

The power coefficient of the rotor alone is also compared with

Table 5
Comparison of C_p with previous prototype tests.

	Jeffcoate et al. (Jeffcoate et al., 2016)	Atcheson et al. (Atcheson et al., 2015)	Present study
Test type	Prototype	Prototype	Prototype
Test facility	Field test	Field test	Towing tank
Rotor diameter (m)	1.5	1.5	1.2
Speed (m/s)	**1.0**	**1.1**	**0.5**
C_p	0.34	0.33	0.33
TSR	3	3.1	5.37

Table 6
Comparison of C_p with previous rotor tests.

		Bahaj et al. (Bahaj et al., 2007)	Mycek et al. (Mycek et al., 2014a)	Doman et al. (Doman et al., 2015)	Seo et al. (Seo et al., 2016)	Morandi et al. (Morandi et al., 2016)	Present study
Test type		Rotor	Rotor	Rotor	Rotor	Rotor	Rotor
Test facility		Water tunnel	Towing tank	Towing tank	Towing tank	Water channel	CFD
Rotor diameter (m)		0.8	0.7	0.762	0.4	0.402	1.2
High speed test	Speed (m/s)	1.73	1.2	1.0	1.436	2.76	−
	C_p	0.46	0.44	0.285	0.278	0.39	−
	TSR	6	4.8	3.53	3.5	2.6	−
Low speed test	Speed (m/s)	−	0.4	0.5	−	−	0.5
	C_p	−	**0.36**	**0.075**	−	−	**0.41**
	TSR	−	3	4.06	−	−	5

the experimental data from previous literature, as listed in Table 6. The optimal C_p of the rotors is in the range of 0.285 (Doman et al. (2015).) to 0.46 (Bahaj et al. (2007).). It should be noted that all the previous rotors obtain the optimal C_p at relative higher flow velocities. For example, the rotor of Mycek et al. (2014a). has an optimal C_p of 0.44 at an flow velocity of 1.2 m/s. However, the power coefficient drops to 0.36 at 0.4 m/s. The decrease in performance is more significant in the experiment of Doman et al. (2015). By comparing the performance of current rotor with that tested by Mycek et al. (2014a). at 0.4 m/s, it can be found that the current rotor has a maximum coefficient of power of 0.41 at $TSR = 5$, which is 13.9% higher for the low-velocity flow condition (0.5 m/s).

6. Conclusions

A horizontal axis hydrokinetic turbine is designed for low flow speed power generations. To reduce the friction caused by the mechanical seals, a magnetic coupling is used for the transmission of the rotor torque. A prototype turbine is manufactured and tested in the towing tank to verify the feasibility of using magnetic couplings in the torque transmission. The performance of the prototype, including power, torque, thrust and wake characteristics is then studied using a three dimensional CFD method. The main conclusions of this study include:

(1) The designed turbine characterized a cut-in velocity of 0.25 m/s, which is considerable lower than common tidal turbines. So the feasibility of using magnetic couplings to reduce the resistive torque in the transmission parts is proved. This finding is very helpful for the future design of small-to-mid scale hydrokinetic turbines, because we can use properly designed magnetic couplings for the non-contacting torque transmission and eliminating the mechanical seals.
(2) The designed turbine characterized a maximum power coefficient of 0.33. Although this value is lower than that obtained by the CFD (0.41), it is satisfying considering the low flow velocity (0.5 m/s) and the small hydrodynamic forces on the rotor. The generator in the current design, Maxon 35 L, is often used as a motor rather than a generator. Therefore, the power coefficient of the turbine could be further increased by replacing the current gearbox and the generator with a more specifically designed substitute whose rated speed and power could match perfectly with the rotor.
(3) The CFD simulations shows the wake structures and the flow around the blades of the turbine. When the rotor is rotating, the flow separates from both the tip and the root of the blade like two concentric spiral lines. While when the rotor is fixed, the flow separates directly from both the leading edge and the trailing edge of the blade and forms a wake similar to the Karman vortex street.

References

Alstom, 2013. Alstom's Tidal Turbine Reaches 1MW in Offshore Conditions. http://www.alstom.com/press-centre/2013/7/alstoms-tidal-turbine-reaches-1mw-in-offshore-conditions/. Accessed on 7 6 2017.
Althaus, D., 1996. Niedriggeschwindigkeitsprofile. Friedr Vieweg & Sohn Verlagsgesellschaft mbH Braunschweig/Weisbaden, Germany.
ANSYS, 2011. ANSYS 15.0 User's Guide.
Atcheson, M., Mackinnon, P., Elsaesser, B., 2015. A large scale model experimental study of a tidal turbine in uniform steady flow. Ocean. Eng. 110, 51–61.
Bahaj, A.S., Molland, A.F., Chaplin, J.R., et al., 2007. Power and thrust measurements of marine current turbines under various hydrodynamic flow conditions in a cavitation tunnel and a towing tank. Renew. Energ 32 (3), 407–426.
Belloni, Clarissa, S.K., 2013. Hydrodynamics of Ducted and Open-centre Tidal Turbines. University of Oxford.
Cresswell, N.W., Ingram, G.L., Dominy, R.G., 2015. The impact of diffuser augmentation on a tidal stream turbine. Ocean. Eng. 108 (12), 155–163.
Doman, D.A., Murray, R.E., Pegg, M.J., Nevalainen, T., et al., 2015. Tow-tank testing of a 1/20th scale horizontal axis tidal turbine with uncertainty analysis. Int. J. Mar. Energ 11, 105–119.
Fleming, C.F., Mcintosh, S.C., Willden, R.H.J., 2011. Design and analysis of a bi-directional ducted tidal turbine. In: European Wave and Tidal Energy Conference, Southampton, UK.
Fleming, C.F., Willden, R.H.J., 2016. Analysis of bi-directional ducted tidal turbine performance. Int. J. Mar. Energ 16, 162–173.
Gaden, D.L.F., Bibeau, E.L., 2010. A numerical investigation into the effect of diffusers on the performance of hydro kinetic turbines using a validated momentum

source turbine model. Renew. Energ 35 (6), 1152—1158.

Galloway, P.W., Myers, L.E., Bahaj, A.B.S., 2011. Experimental and Numerical Results of Rotor Power and Thrust of a Tidal Turbine Operating at Yaw and in Waves. World Renewable Energy Congress, Sweden, pp. 2246—2253.

Gu, Y., Zhao, G., LIU, H., et al., 2013. Characteristics of drag reduction of bionic dimpled surface of shell rubber ring of aerodynamic extinguishing cannon. J. Jilin Univ. 43 (4), 983—990.

Jeffcoate, P., Whittaker, T., Boake, C., et al., 2016. Field tests of multiple 1/10 scale tidal turbines in steady flows. Renew. Energ 87, 240—252.

Lawson, M.J., Li, Y., Sale, D.C., 2011. Development and Verification of a Computational Fluid Dynamics Model of a Horizontal-Axis Tidal Current Turbine. Office of Scientific & Technical Information Technical Reports.

Lee, N.J., Kim, I.C., Chang, G.K., et al., 2016. Performance study on a counter-rotating tidal current turbine by CFD and model experimentation. J. Mech. Sci. Technol. 30 (2), 519—524.

Liu, J., Lin, H., Purimitla, S.R., 2016. Wake field studies of tidal current turbines with different numerical methods. Ocean. Eng. 117, 383—397.

Liu, Z., Wang, H., 2014. Effect of bionic concave surface to the drag reduction performance of cylinder sealing ring. Adv. Mater. Res. 1055, 152—156.

Louise, K., Bjoern, E., Robert, K., et al., 2016. Do changes in current flow as a result of arrays of tidal turbines have an effect on Benthic communities? Plos One 11 (8), e0161279.

Luquet, R., Bellevre, D., Fréchou, D., et al., 2013. Design and model testing of an optimized ducted marine current turbine. Int. J. Mar. Energ 2, 61—80.

Maxon, 2017. Maxon Motor. http://www.maxonmotor.com/maxon/view/content/products. Accessed on 7 6 2017.

MCT, 2017. SeaGen Technology. http://www.marineturbines.com/Seagen-Technology. Accessed on 7 6 2017.

Morandi, B., Felice, F.D., Costanzo, M., et al., 2016. Experimental investigation of the near wake of a horizontal axis tidal current turbine. Int. J. Mar. Energ 14, 229—247.

Mycek, P., Gaurier, B., Germain, G., et al., 2014a. Experimental study of the turbulence intensity effects on marine current turbines behavior. Part I: one single turbine. Renew. Energ 66, 729—746.

Mycek, P., Gaurier, B., Germain, G., et al., 2014b. Experimental study of the turbulence intensity effects on marine current turbines behaviour. Part II: two interacting turbines. Renew. Energ 68, 876—892.

Sale, D.C., 2014. NWTC Information Portal (HARP_Opt). https://nwtc.nrel.gov/HARP_Opt. Accessed on 7 6 2017.

Schleicher, W.C., Riglin, J.D., Oztekin, A., 2014. Numerical characterization of a preliminary portable micro-hydrokinetic turbine rotor design. Renew. Energ 76, 234—241.

Seo, J., Lee, S.J., Choi, W.S., et al., 2016. Experimental study on kinetic energy conversion of horizontal axis tidal stream turbine. Renew. Energ 97, 784—797.

Shives, M., Crawford, C., 2010. Overall Efficiency of Ducted tidal current turbines. Oceans 2010, 1—6.

Tatum, S., Allmark, M., Frost, C., et al., 2016. CFD modelling of a tidal stream turbine subjected to profiled flow and surface gravity waves. Int. J. Mar. Energ 15, 156—174.

Tethys, 2011. HS1000 at EMEC. https://tethys.pnnl.gov/annex-iv-sites/hs1000-emec. Accessed on 7 6 2017.

Tian, W., Vanzwieten, J.H., Pyakurel, P., et al., 2016. Influences of yaw angle and turbulence intensity on the performance of a 20kW in-stream hydrokinetic turbine. Energy 111, 104—116.

UIUC, 2011. Airfoil Coordinates Database. University of Illinois at Urbana-Champaign. http://m-selig.ae.illinois.edu/ads/coord_database.html#F. Accessed on 7 6 2017.

Wang, S., Yuan, P., Li, D., et al., 2011. An overview of ocean renewable energy in China. Renew. Sust. Energy Rev. 15 (1), 91—111.

Wang, S.Q., Sun, K., Xu, G., et al., 2016. Hydrodynamic analysis of horizontal-axis tidal current turbine with rolling and surging coupled motions. Renew. Energy 102, 87—97.

Xu, G., Zhao, J., Zhao, G., et al., 2015. Drag reduction characteristic of bionic non-smooth seal ring for cylinder. Chin. Hydraul. Pneum. (1), 96—100.